Modification of Transition-Metal Redox by Interstitial Water in Hexacyanometallate Electrodes for Sodium-Ion Batteries

Jinpeng Wu[†, #], Jie Song[‡], Kehua Dai[※, #], Zengqing Zhuo[§, #], L. Andrew Wray[⊥], Gao Liu[#], Zhi-xun Shen[†], Rong Zeng[*, ∥], Yuhao Lu[*, ‡], Wanli Yang[*, #]

[†]Geballe Laboratory for Advanced Materials, Stanford University, Stanford, California 94305, USA

[#]Advanced Light Source, Lawrence Berkeley National Laboratory, Berkeley, California 94720, United States [‡]Novasis Energies, Inc., Vancouver, Washington, 98683, United States

[※]School of Metallurgy, Northeastern University, Shenyang 110819, China

[§]School of Advanced Materials, Peking University Shenzhen Graduate School, Shenzhen 518055, China

[⊥]Department of Physics, New York University, New York, New York 10003, United States

[∥]Department of Electrical Engineering, Tsinghua University, Beijing 100084, China

ABSTRACT

A Sodium-ion battery (SIB) solution is attractive for grid-scale electrical energy storage. Low-cost hexacyanometallate is a promising electrode material for SIBs because of its easy synthesis and open framework. Most hexacyanometallate-based SIBs work with aqueous electrolyte and interstitial water in the material has been found to strongly affect the electrochemical profile, but the mechanism remains elusive. Here we provide a comparative study of the transition-metal redox in hexacyanometallate electrodes with and without interstitial water based on soft X-ray absorption spectroscopy and theoretical calculations. We found distinct transition-metal redox sequences in hydrated and anhydrated $Na_xMnFe(CN)_6 \cdot zH_2O$. The Fe and Mn redox in hydrated electrodes are separated and at different potentials, leading to two voltage plateaus. On the contrary, mixed Fe and Mn redox at the same potential range is found in the anhydrated system. This work reveals for the first time that transition-metal redox in batteries could be strongly affected by interstitial molecules that are seemingly spectators. The results suggest a fundamental

mechanism based on three competing factors that determine the transition-metal redox potentials. Because most hexacyanometallate electrodes contain water, this work directly reveals the mechanism of how interstitial molecules could define the electrochemical profile, especially for electrodes based on transition-metal redox with well-defined spin states.

INTRODUCTION

The rapid development of the generation of electrical energy from renewable but variable solar and wind power has led to an urgent demand for an economic mean of storing large-scale electric energy to enable its smooth integration into the grid.[1] Rechargeable batteries are promising solutions for such grid-scale electrical-energy storage, if a stable and low-cost battery technology could be developed. Although lithium-ion batteries (LIBs) have been ubiquitous in portable electronics and electric vehicles, the use of lithium for grid-scale storage is limited by cost and supply restriction.[2] In the meantime, a room-temperature sodium-ion battery (SIB) solution for large-scale storage of electrical energy has attracted more and more research interests, however still requires tremendous efforts in both fundamental understanding and practical developments to meet the formidable challenges on the low-cost, stability, safety and rate performance for grid-scale storage.[3-5]

Hexacyanometallates, with a universal nominal formula $A_xM_a[M_b(CN)_6]_y{\cdot}zH_2O$ (A=alkali and alkaline metal ions; M_a and M_b=transition-metal (TM) ions; $0 \leq x \leq 2$; $y \leq 1$), have long been investigated as promising hosts for alkali and alkaline ions.[6-7] Recently, the materials are revisited as SIB cathodes in both aqueous[8-11] and non-aqueous[12-15] electrolytes, owing to their easy synthesis, low cost and open framework with large interstitial space for sodium-ions. Extensive efforts have been made to improve the performance, especially the capacity and cyclability of hexacyanometallate-based electrodes for SIBs. One of the typical

practices is to substitute the Fe in the so-called Prussian Blue (PB) $AFe^{III}Fe^{II}(CN)_6$ to obtain Prussian Blue Analogue (PBA) materials, i.e., $AMFe(CN)_6$ with M being different kinds of TMs including Mn, Co, Ni, Cu and Zn.[11-12] The two Fe atoms in the PB molecule could also be replaced by Mn.[16] All these efforts are based on the mechanism that electrochemical performance of hexacyanometallate electrodes is based on well-defined TM redox couples.[11, 17] Therefore, performance of the SIBs could be optimized through the modification of the TM redox in hexacyanometalate electrodes.

Additionally, various insertions into the interstitial space of hexacyanometallate electrodes through synthesis lead to strong effect on the electrochemical characteristics of the SIBs, such as Columbic efficiency and charge/discharge profiles. For example, Wessells *et al*. investigated Li^+, Na^+, K^+ and NH_4^+ insertions into $KMFe(CN)_6$ with M = Cu and Ni using aqueous electrolyte.[8, 18-19] You *et al*. found that the variation of Na content in $Na_xFe[Fe(CN)_6]$ results in a rhombohedral to cubic phase transition of the material.[20] In general, lattice water has been found to be important on the electrochemical performance in various battery electrodes.[21-25] In particular for PBA materials, other than the structural changes, Song *et al*. reported a rather intriguing effect of the interstitial H_2O on the charge/discharge characteristics of $Na_xMnFe(CN)_6{\cdot}zH_2O$ (Na_2MnHFC).[26] When the interstitial water is removed from the material, the electrochemical behavior is greatly improved, changing from a two-plateau to a single-plateau profile with much reduced polarization.[26] It is thus evident that controlling the interstitial molecule could play a critical role in modifying and/or optimizing the electrochemical performance of hexacyanometallate electrodes for SIBs. However, this intriguing phenomenon is yet to be understood, and the change of TM redox in electrodes with and without interstitial molecules is yet to be detected and clarified. In particular, the understanding of how the well-separated $Mn^{2+/3+}$ and $Fe^{2+/3+}$ redox potentials could be completely merged together by removing just interstitial water remains elusive.[26] A direct probe to

clarify the modification of the TM redox by interstitial water molecule, i.e., TM redox in the hydrated and anhydrated Na_2MnHFC, holds the key to answer the important question of the interstitial molecule effect on electrochemical performance.

In this work, we provide a direct probe with quantitative analysis of the Mn and Fe redox sequence in the hydrated and anhydrated Na_2MnHFC electrodes through synchrotron-based soft X-ray absorption spectroscopy (sXAS) and theoretical calculations. We quantitatively analyze the TM redox couples in the materials with and without interstitial water, thus directly reveal how the interstitial water modifies the TM redox and then the electrochemical profile. Our results clarify unambiguously the effect of an interstitial molecule on the modification of the spin-state related TM redox in a SIB cathode material. We suggest that the electrochemical profile of such SIB electrode depends on three correlated parameters: the conventionally considered ionization energies of TMs, the fundamental spin states of the TMs, and the crystal field that depends on the structure and interstitial molecules.

EXPERIMENTAL AND THEORETICAL SECTION

Two sets of $Na_xMnFe(CN)_6 \cdot zH_2O$ materials are prepared, hydrated and anhydrated. The as-prepared $Na_xMnFe(CN)_6$ precipitate was separated into two parts; both parts were dried at 100 ℃, one under air and the other under vacuum. By thermogravimetric analysis (TGA) on the two sets of samples, the nominal parameter of the H_2O content z in the hydrated phase is 1.87, while that in the anhydrated phase is 0.3. As determined through inductively coupled plasma (ICP) analysis, both white powder samples have the same molar Na/Fe/Mn ratio of 1.89:0.97:1.00. The hydrated and anhydrated samples show monoclinic and rhombohedral phases, respectively.[26]

Figure 1(a) shows the typical electrochemical profile of the first cycle of the two

systems. The hydrated sample exhibited two plateaus locating at 3.45V/3.79V on the charge curve and 3.17V/3.49V on the discharge curve, whereas the anhydrated exhibited a single one locating at 3.53V on the charge curve and 3.44V on the discharge curve. The structural and electrochemical profile studies are consistent with previous reports,[19, 26] and are not the topics of this work; but for the convenience of the readers, we have included all the information in the supplementary materials (Fig. S1 and S2). In this study, we select five representative states of charge (SOC) for both the hydrated and the anhydrated samples: 0% (H1 and AH1), 25% (H2 and AH2), 50% (H3 and AH3), 75% (H4 and AH4) and 100% (H5 and AH5), as marked in Figure 1(a).

sXAS is performed in the newly commissioned iRIXS endstation at beamline 8.0.1 of the Advanced Light Source.[27] Samples are loaded in our Ar glove box through a home-made sample transfer kit without any air exposure throughout the process.[28] In order to avoid the irradiation damage effect, the X-ray beam is defocused for experiments here, and the samples are cooled down with liquid N_2 while collecting the spectra.

sXAS has been demonstrated as a powerful technique to probe the critical states in various battery compounds.[29] For TMs, because sXAS is a direct probe of the TM *3d* states through the strong dipole-allowed *2p-3d* (L-edge) excitations, TM L-edge sXAS is extremely sensitive to the evolution of the TM states involved in a typical battery electrode, e.g., Ni,[30] Co,[31] Fe,[32-33] and Mn.[30, 34] By virtue of the high sensitivity and the well-defined multiplet features of TM L-edge sXAS to the TM states, sXAS often allows quantitative or quasi-quantitative analysis of the TM redox in electrodes upon electrochemical cycling.[35] Particularly for hexacyanometallate based electrodes, we have shown previously that TM-L spectral lineshape depends strongly on the spin states of the TMs,[11, 34] Compared with other oxide based battery electrodes, TM redox analysis in hexacyanometallate involves distinct sXAS lineshape for the same

TM redox with different spin states at different sites; however, these previous works set a solid foundation for our quantitative and comparative analysis of the Fe and Mn redox in hydrate and anhydrate $Na_xMnFe(CN)_6 \cdot zH_2O$ systems.

The quantitative analysis of the Fe and Mn oxidation state based on sXAS results is performed with the following two steps. First we analyze the contents of TM oxidation states of the two end-members, i.e., the fully charged and discharged electrodes, by comparing the intensity of the characteristic sXAS features with theoretical calculations. Details on the selection of the energy range and the interpretation of the results are elaborated in the sessions of Results and Discussions below. Second, we used the linear combination of the experimental spectra of the two end-members to fit all the intermediated states with a single fitting parameter, i.e., the ratio of the two end-members. This fitting is performed in all the four sets of experimental data, i.e., Fe and Mn spectra of the anhydrated and hydrated systems, with a high R-factor values (Supplementary Table S1) indicating the high accuracy of the fittings.

Theoretically, Fe-*L* and Mn-*L* sXAS of hexacyanometallate can be accurately modeled by atomic multiplet calculations augmented to include both forward and back bonding.[36-37] Such an approach allows a direct assignment of the spectroscopic features to the specific site and the spin state of Fe and Mn atoms. The calculations in this paper follow the approaches developed by Hocking *et al*,[36] which was successfully applied in the previous works.[11, 34] By comparing with our experimental results, we are able to adjust the hopping parameters and back-bonding configuration energies to reproduce the energy splittings observed in the sXAS experiments. The combination of experiments and theory then provide a reliable analysis of the TM redox in the electrodes with well-defined spin states.

RESULTS AND DISCUSSIONS

Benchmark of $Fe^{2+/3+}$ and $Mn^{2+/3+}$ with distinct spin states. Aiming at a quantitative analysis on the TM redox in $Na_{2-x}Mn[Fe(CN)_6]$, characteristic sXAS features corresponding to different TM valence states with specific spin states need to be determined. In general, hexacyanometallates are known as SIB cathodes with redox couples of TM bivalent and trivalent states at fully discharged (Alkali ion intercalated) and charged (Alkali ion deintercalated) states, respectively. i.e., Fe^{2+} and Mn^{2+} in a fully discharged $Na_{2-x}Mn[Fe(CN)_6]$ (H1 and AH1), and Fe^{3+} and Mn^{3+} in a fully charged state (H5 and AH5). Additionally, the spin states of the TMs in hexacyanometallates are also known to be determined by the different crystal field strength at the C- and N-coordinated sites. The structure of hexacyanometallates consists of a double-perovskite framework with $(C{\equiv}N)^-$ anions bridging TM-N_6 and TM-C_6 octahedra. The strong crystal field at the C-coordinated site leads to a large splitting of the $3d_{t2g}$ and $3d_{e*g}$ states of the TM and a well-defined low-spin (LS) state. On the contrary, the TM is in the high-spin (HS) state at the N-coordinated TM-N_6 octahedron due to the relatively weak crystal field.[38-40]

Figure 1(b) and (c) show the sXAS of Fe and Mn L_3-edges of the fully charged and discharged $Na_{2-x}Mn[Fe(CN)_6]$ samples with (H5, H1) and without (AH5, AH1) interstitial water. The L_3-edge sXAS spectra consist of distinct features resulting from the multiplet-effect coupling between the *2p* core-hole and *3d* states.[41] These well-defined features allow an unambiguous definition of the oxidation states by comparing the theoretical calculations of Fe and Mn L_3-edge sXAS with our experimental data. For the two sets of fully charged/discharged electrodes, all the sXAS experimental features could be reproduced by theoretical calculations of LS Fe and HS Mn with the expected valences, as shown in Figure 1(b) and (c). We note that features of Fe and Mn at the other spin states have been reported before,[11, 34] (Supplementary Fig. S3), but are not observed here. Therefore, the sXAS of these end-members provides the direct experimental evidence that the Fe and Mn in $Na_{2-x}Mn[Fe(CN)_6]$ are at the C- and N-

coordinated sites, and take LS and HS states, respectively.

An important aspect of the spin-state effect on electrochemical property is revealed by our sXAS results here (red arrow in Fig. 1b). Naively, because sXAS corresponds to the unoccupied states, which indicates the empty states that could be filled up during the intercalation (discharge of cathode) process.[42] In Figure 1(b), a striking feature at 707.1 eV can be seen for LS Fe^{3+}. This feature sits at a significantly low energy, and is associated with back-bonding to the π-bonding hole in the t^5 configuration of the $Fe^{III}C_6$ octahedra: t^5e^0. The low energy 707.1 eV state thus originates from the t_{2g} hole when going from the fully-filled t_{2g} LS Fe^{2+} to LS Fe^{3+} during the charge process. Because of the low energy of this unoccupied state, it is favored in energy to prioritize the filling of this state during the discharge (reduction) process, i.e., the potential of LS $Fe^{2+/3+}$ will be shifted higher because of the low-spin nature of C-coordinated Fe. We note that such a simple atomic analysis has successfully explained the two voltage plateaus of the same $Fe^{2+/3+}$ redox at different sites in rhombohedral Prussian White electrodes.[34] We also note that such a distinct low-energy state in sXAS is not observed for the Mn as displayed in Fig. 1c. Therefore, the low-spin configuration of the Fe fundamentally increases its relative electrochemical potential, as will be elaborated later in this work.

The well-defined features of the LS Fe and HS Mn in the sXAS data allow us to establish the benchmarks for further quantitative analysis of the Fe and Mn oxidation states. For Fe states, the specific origin of the 707.1 eV peak in the LS Fe^{3+} system also leads to the quantitative discrepancy on the peak intensity between the experiment and theory (Figure 1b). It is obvious that the sharpness and height of this peak is exaggerated in experiments, likely due to a different life-time of such specific low-energy feature in spectroscopy, which is not considered in theory. Therefore, later in this work, we have chosen the energy range from 709 to 715 eV for the quantitative analysis of the intermediated

states, which contains defined features of both Fe^{2+} and Fe^{3+}. Nonetheless, we note that the intensity evolution of the 707.1 eV peak follows the same trend qualitatively. As shown in Figure 1b, the spectra of H1/AH1 samples represent the standards for LS Fe^{2+}, and spectra of H5/AH5 represent LS Fe^{3+}. For Mn states, H1/AH1 samples display the standard HS Mn^{2+} lineshape. However, significant contributions from Mn^{2+} (640 eV) could be observed in the H5/AH5 samples (Fig. 1c). So we reproduce the ratio of Mn^{2+} (640 eV) and Mn^{3+} (642.2 eV) features by linear combination of the calculated spectra. A content of 0.48 and 0.55 Mn^{3+} in hydrated and anhydrated samples are found (Supplementary Fig. S4). Because sXAS is a surface sensitive probe, this result indicates a reduced electrode surface that has been reported in many other Mn-based battery electrodes[30], however has never been reported for PBAs. We suspect this surface reduction contributes to the capacity loss of these electrodes when compared with the theoretical capacity. Below we analyze the Fe and Mn redox reactions at different electrochemical stages by using the experimental spectra of the four end members analyzed here.

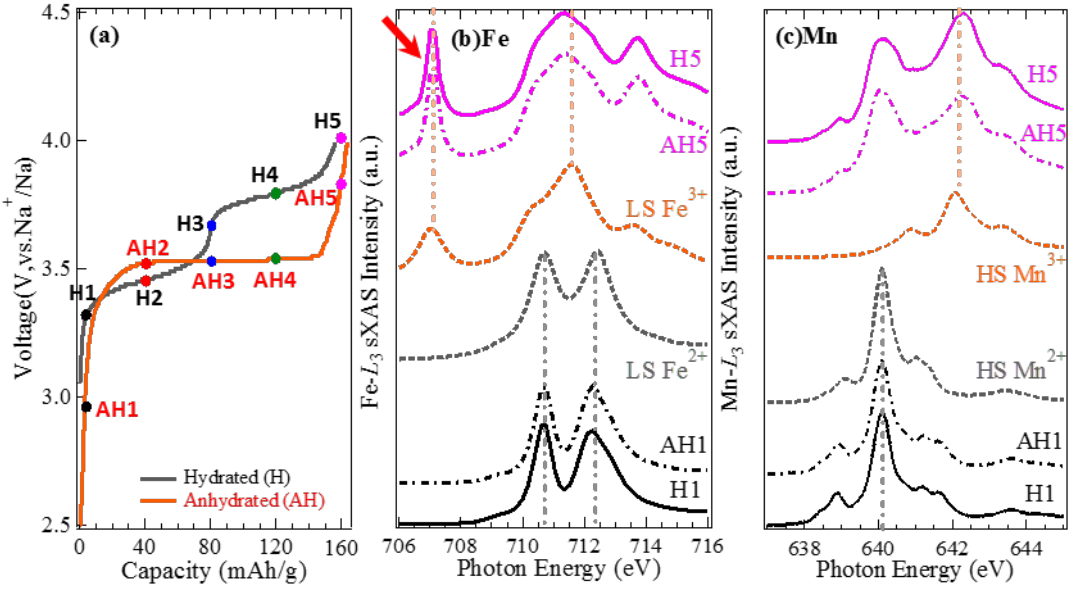

Figure 1. (a) Two sets of samples with five different SOCs are defined here for hydrated (H1 to H5) and anhydrated (AH1 to AH5) systems. (b) and (c) Experimental Fe and Mn L_3-edge sXAS spectra are compared with calculated spectra of LS Fe^{2+}/Fe^{3+} and HS Mn^{2+}/Mn^{3+}, respectively. All spectral features are clearly interperated by LS Fe and HS Mn calculations. Features from other valence and spin state configurations (Fig. S3) are not observed here. Red arrow indicates the specific low energy features of LS Fe^{3+}, which is favored in energy during the oxidation process, i.e., high potential (see text).

Fe Redox Activity. Figure 2 shows the Fe L_3-edge sXAS spectra collected on a series of electrode samples with different SOCs. The spectra evolve with electrochemical cycling, corresponding to the change of Fe oxidation states. As elaborated above, the fully discharged/charged electrodes display the characteristic lineshape of LS $Fe^{2+/3+}$ and HS $Mn^{2+/3+}$, and they are almost identical for hydrated (H1, H5) and anhydrated (AH1, AH5) samples. Here we focus on the evolution of the sXAS lineshape of the intermediate states to distinguish the distinct Fe redox behavior in the hydrated and anhydrated systems.

Overall, the evolution of Fe L_3 spectra is indicated by two parts: i) the changing lineshape at 710-714 eV, and ii) the increasing intenisty of the 707.1 eV peak (vertical lines in Fig. 2). For both parts, the general lineshape of the 50% SOC hydrated sample (H3) is almost identical to the fully charged one (H5) (Figure 2a), suggesting that the $Fe^{2+/3+}$ redox reaction has been completed at the low voltage plateau from H1 to H3 (Figure 1a). In contrast, for the anhydrated system, the spectral linsehape changes continuously from AH1 to AH5, indicating a gradual change of the Fe state throughout the charging process.

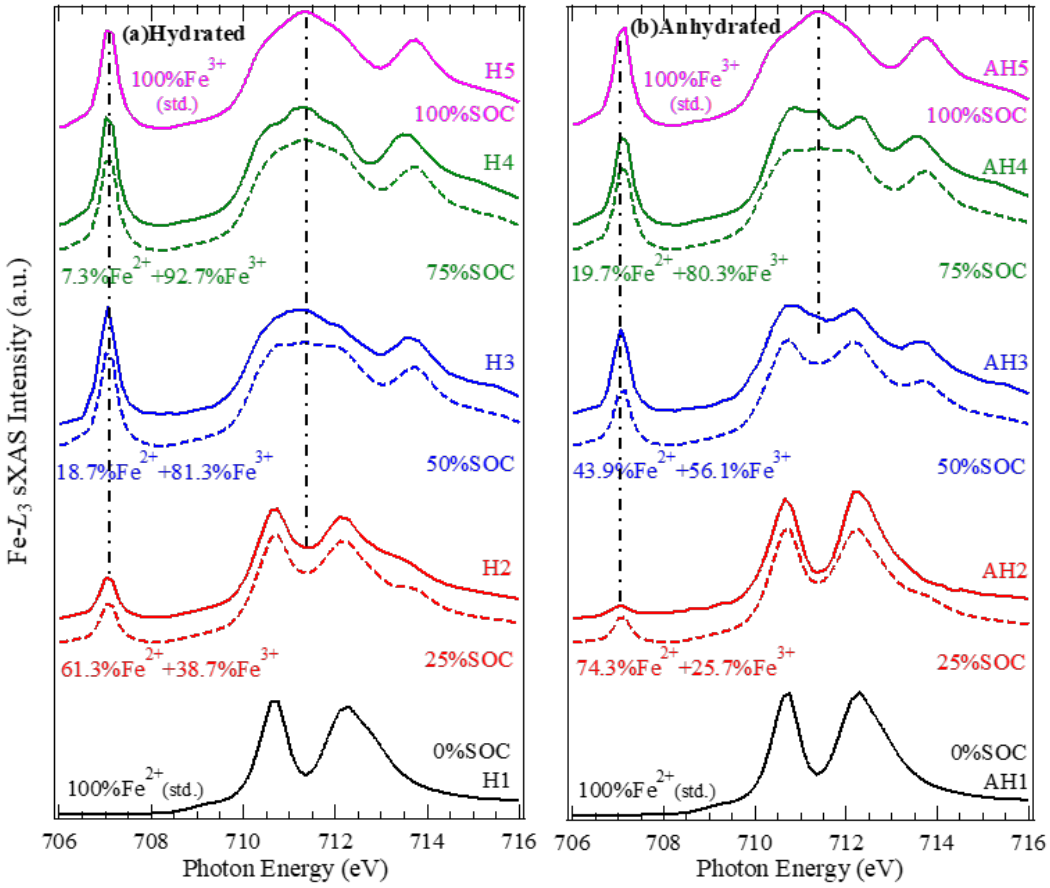

Figure 2. Fe L_3-edge sXAS spectra collected on a series of electrode samples cycled to different SOCs: (a) hydrated samples; (b) anhydrated samples. Dashed lines are calculations of intermediated state by a simple linear combination of the spectra of fully charged/discharged samples.

In order to quantify the Fe redox process, we fit the intermediated spectra by linearly combining the two standard spectra from the fully charged/discharged samples. As described above, the experimantal spectra of H1/AH1 and H5/AH5 represent the standard spectra of Fe^{2+} and Fe^{3+}, respectively, and we fit the spectra at the 709 – 715 eV energy range. This simple linear cimbination provides a fairly good fitting to our experimental results (dashed lines in Fig. 2), and the derived Fe valence concentration is noted in Figure. 2 under each set of spectra. The quantitative analysis shows again that the 0-50% SOC (low plateau) corresponds to an almost complete (98%) Fe oxidation to Fe^{3+} in the

hydrated system, but about exactly 50% Fe oxidation in the anhydrated system.

Mn Redox Activity. Figure 3 shows the Mn L_3-edge sXAS spectra collected on a series of electrode samples with different SOCs. Here we could focus on the evolution of the only characteristic feature of Mn^{3+} at 642.3 eV (dashed vertical lines). For the hydrated system, the spectra show no signal of Mn^{3+} at 642.3 eV from 0-50% SOC (H1 to H3), but then rapidly evolved into fully oxidized Mn^{3+} from 50% to 100% SOC (Figure 3a). Again, a simple linear combination of the two end members (Fig. 3a) confirms quantitatively that Mn redox takes place at the high SOC range (high voltage plateau). Although the Mn state does not follow exactly the norminal SOC due to the existence of surface Mn^{2+}, as discussed above for the fully charged samples, it is clear that most Mn oxidation takes place at relatively high SOC regime. Therefore, two separated voltage plateaus of the hydrated electrodes are from the $Fe^{2+/3+}$ redox at low voltage, and $Mn^{2+/3+}$ redox at high voltage.

For unhydrated system, a gradual increase of the Mn^{3+} 642.3 eV signal is observed, similar to the evolution of the Fe sXAS lineshape in unhydrated system. Again, as discussed for the fully charged endmember above, the existence of the surface Mn^{2+} leads to the diviation of the quantative Mn state contents from the SOC. Nontheless, the gradual increase of the Mn^{3+} signal is clear, confirming that the Mn oxidation state gradually increases its valence during the charging process in anhydrated system.

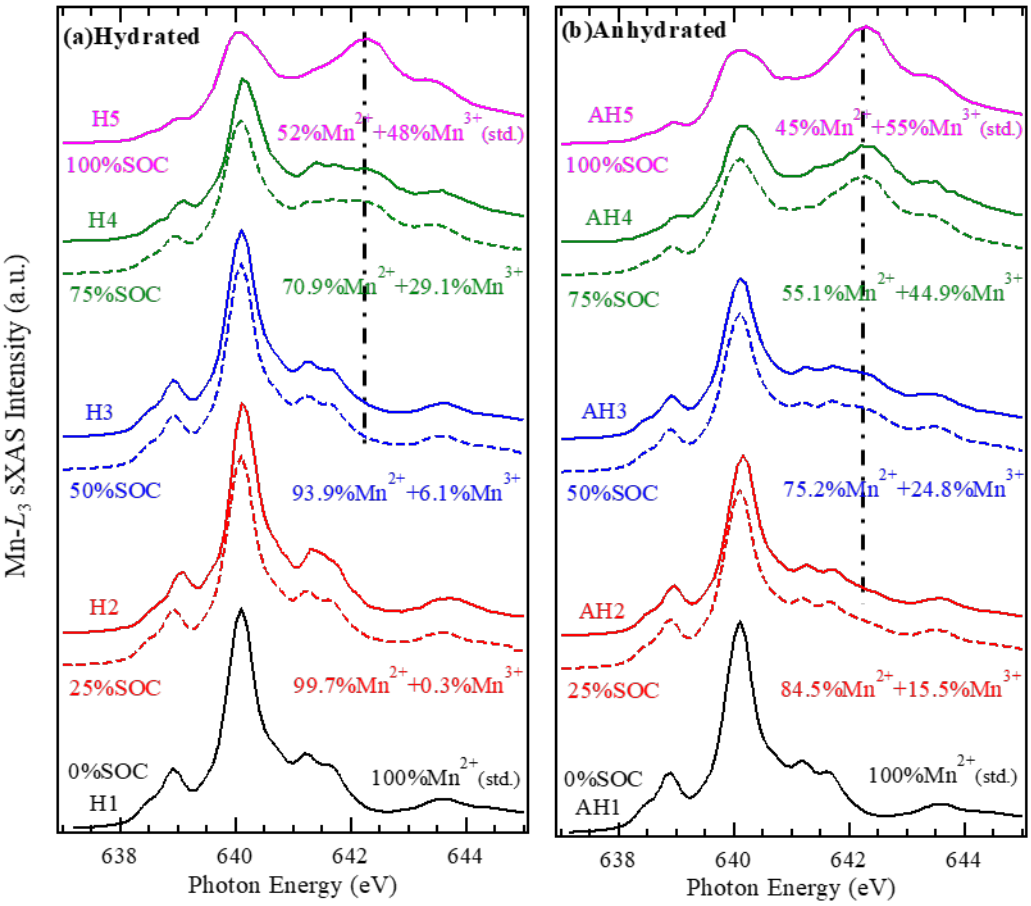

Figure 3. Mn L_3-edge sXAS spectra collected on a series of electrode samples cycled to different SOCs: (a) hydrated samples; (b) anhydrated samples. The calculated spectra are shown in dashed lines.

Effect of Interstitial H_2O on Fe and Mn Redox. Based on the analysis above, the different Fe and Mn redox sequence in the hydrated and anhydrated cathode materials are clarified. Figure 4 is a summary of the valence concentration of the oxidized Fe^{3+} and Mn^{3+} upon electroehcmical cycling in the two comparative systems. For the hydrated system, $Fe^{2+/3+}$ and $Mn^{2+/3+}$ redox reations take place separatedly at the first (low potential) and second (high potential) half of the charging process, leading to two separated voltage plateaus (Figure 4a). However, for the anhydrated system, both Fe and Mn display a gradual increase on their oxidation state roughly following the SOC

changes, i.e., a mixed Fe/Mn redox reaction throughout the electrochemical process. Such a mixed redox reaction leads to the dissapearance of the two distinct plateau as for hydrated system.

The modification of the TM redox, and thus the electrochemical profile, by interstitial water is a nontrivial phenomenon, which indeed leads to distinct battery performance[26]. The clarification of the underlying redox mechanism here reveals an intriguing effect of interstitial water molecule in $Na_xMnFe(CN)_6 \cdot zH_2O$ for SIBs. The distinct TM redox sequence in the contrasting systems indicates effects from several competing factors for determining the electrochemical properties: the spin states, the crystal field (structure), and the oxidation energy of TMs. Additionally, the structural change by introducing interstitial water also plays important roles in defining the electrochemical profile.

First, in the conventional wisedom, the redox potential depends on the ionization energy of the TM with particular oxidation states. The standard ionization energy of Fe^{2+} is lower than that of Mn^{2+}, which means Fe^{2+} is easier to be oxidized than Mn^{2+}.[43] Therefore the standard electrode potential of Fe^{2+} is usually lower than that of Mn^{2+}, as observed before in SIB cathodes.[44-46] Second, in $Na_xMnFe(CN)_6$ materials, Fe and Mn are coordinated with $(C{\equiv}N)^-$ and $(N{\equiv}C)^-$, respectively. As expected and directly probed in this work, the C-coordinated Fe is at LS state, and the N-coordinated Mn is at HS state. The ligand field stablization energy (LFSE) of LS Fe^{2+} is higher than that of HS Mn^{2+},[47] leading to the increase of $Fe^{2+/3+}$ redox potential. Note this is consistent with the sXAS finding of the low-energy state of LS Fe^{3+}, as elaborated above (red arrow in Fig. 1b). If the competing effects of the ionization energy (low $Fe^{2+/3+}$ redox potential) and LFSE (high $Fe^{2+/3+}$ redox potential) balance each other, the (LS) Fe^{2+} and (HS) Mn^{2+} redox potentials would overlap, leading to a single plateau structure of the electrochemical profile in a “pristine” (anhydrated) $Na_xMnFe(CN)_6$ system.

Third, the balance of the competing effect from the LFSE with specific spin states and the ionization energy could be easily broken by the change of structure and/or crystal field strength of the materials, in which, inerstitial molecules could play a critical role. The interstitial water molecules in the hydrated system dilutes the ligand field in the FeC_6 and MnN_6 octahedra[43], and disturb the original structure that defines the spin states.[26] Additionally, a lattice extension with intersticial water has been found before,[26] and structural changes are also known to affect the electrochemical potential in battery electrodes. When the weakened LFSE effect cannot compete with the ionization energy, the potential gap of the conventional $Fe^{2+/3+}$ and $Mn^{2+/3+}$ redox re-emerges, leading to a two-plateau structure in the electrochemical profile of the hydrated electrodes. We note that quantitative analysis of these three important factors deserves further comprehensive theoretical calculations. Nontheless, this scenario is directly supported by the different TM redox sequence revealed in this work.

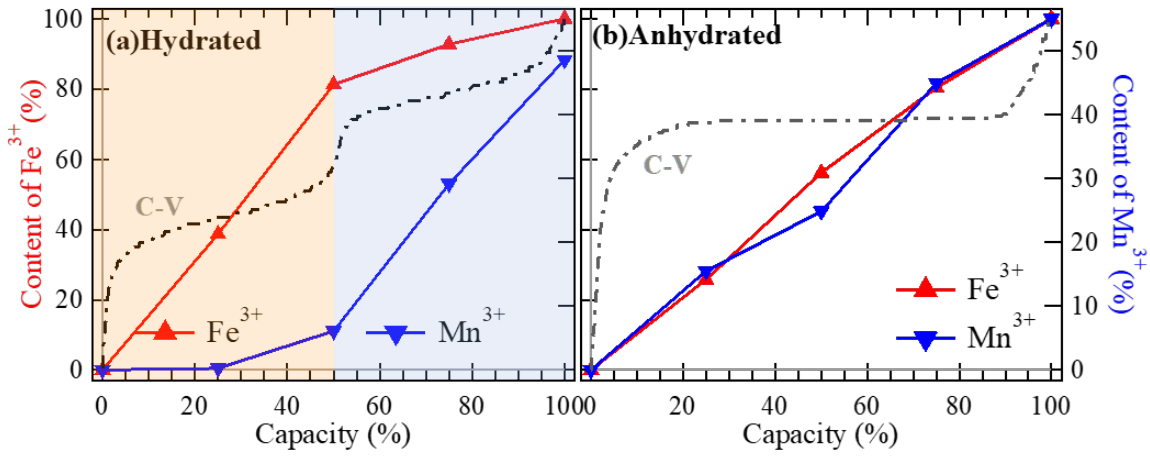

Figure 4. The concentration of the oxidation states of Fe^{3+} and Mn^{3+} upon electrochemical potentials. Percentage of the oxidized TM^{3+} states in the hydrated samples (a) and anhydrated samples (b) directly represents the distinct TM redox sequence in the two systems.

CONCLUSIONS

We have performed a comprehensive analysis of the $Fe^{2+/3+}$ and $Mn^{2+/3+}$ redox sequence in $Na_xMnFe(CN)_6$ with and without interstitial water through sXAS experiments and theoretical calculations. Our results clearly show that the contrast on the electrochemical profile of the two systems is due to the separation of the $Fe^{2+/3+}$ and $Mn^{2+/3+}$ redox potentials when interstitial water is introduced into the system. The two-plateau profile of the hydrated system is attributed to the $Fe^{2+/3+}$ redox at the low potential and the $Mn^{2+/3+}$ redox at high potential. In contrast, mixed $Fe^{2+/3+}$ and $Mn^{2+/3+}$ redox reactions take place in the anhydrated system, leading to a single plateau structure of the electrochemical profile. Our findings natually explain the intriguning difference of the charge/dischage profiles between the hydrated and anhydrated $Na_xMnFe(CN)_6 \cdot zH_2O$ electrodes, and provide a reliable scenario to understand the effect of interstitial water on electrochemical behavior of such SIB electrodes. Fundamentally, the well-defined spin states in such electrode systems, i.e., LS Fe and HS Mn, lead to an LFSE effect that competes with the conventional consideration of the $Fe^{2+/3+}$ and $Mn^{2+/3+}$ redox potentials, resulting in the merge of the two potentials in $Na_xMnFe(CN)_6$. Adding the interstitial water weakens the LFSE effect by diluting the ligand field and increasing the lattice constant, resulting in the re-emergence of the gap between the $Fe^{2+/3+}$ and $Mn^{2+/3+}$ redox potentials. Therefore, our work clarifies the effect of interstitial water on modifying the TM redox in the hexacyanometalate electrode system. Technically, our results reveal the underlying mechanism of optimizing SIB performance through interstitial molecules and suggest that the specific spin states of TMs in battery electrodes like hexacyanometallates provides unique opportunities for performance optimization through interstitial molecules.

ASSOCIATED CONTENT

Supporting Information

Table S1: R-factors of the linear combination fitting of the four systems on Fe and Mn edges. **Figure S1:** Galvanostatic initial charge and discharge profiles of (a) hydrated and (b) anhydrated $Na_xMnFe(CN)_6$ at a current of 0.1 C (15 mA·g−1) in the voltage range of 2.0−4.0 V. The derivative curves (d*Q*/d*V*) plotted as a function of *V* are shown as inserts [21]. **Figure S2:** Local structures of (a) hydrated and (b) anhydrated samples, showing the Na^+ displacements and distorted framework, where high-spin Mn^{II} is blue, low-spin Fe^{II} is green, N is silver, C is dark brown, Na is yellow, and H_2O is red [21]. **Figure S3:** Calculated (a) HS $Fe^{2+/3+}$ and (b) LS $Mn^{2+/3+}$ L_3-edge sXAS spectra [11, 17], with the absolute energy values calibrated. **Figure S4:** Estimation of the contents of Mn^{2+} and Mn^{3+} in fully charged (100% SOC) hydrated and anhydrated samples.

AUTHOR INFORMATION

Corresponding Authors
*zengrong@tsinghua.edu.cn (R.Z.) *yuhao.lu@novasis-e.com (Y.L.)
*WLYang@lbl.gov (W.Y.)

ACKNOWLEDGMENTS

The Advanced Light Source is supported by the Director, Office of Science, Office of Basic Energy Sciences, of the U.S. Department of Energy under Contract No. DE-AC02-05CH11231. The theory efforts are supported by the MRSEC Program of the National Science Foundation under Award Number DMR-1420073.

REFERENCES

1. Yang, Z.; Zhang, J.; Kintner-Meyer, M. C.; Lu, X.; Choi, D.; Lemmon, J. P.; Liu,

J., *Chem Rev* **2011,** *111*, 3577-613.
2. Dunn, B.; Kamath, H.; Tarascon, J. M., *Science* **2011,** *334*, 928-35.
3. Kim, S. W.; Seo, D. H.; Ma, X. H.; Ceder, G.; Kang, K., *Adv Energy Mater* **2012,** *2*, 710-721.
4. Palomares, V.; Serras, P.; Villaluenga, I.; Hueso, K. B.; Carretero-Gonzalez, J.; Rojo, T., *ENERG ENVIRON SCI* **2012,** *5*, 5884-5901.
5. Pan, H. L.; Hu, Y. S.; Chen, L. Q., *ENERG ENVIRON SCI* **2013,** *6*, 2338-2360.
6. Imanishi, N.; Morikawa, T.; Kondo, J.; Takeda, Y.; Yamamoto, O.; Kinugasa, N.; Yamagishi, T., *J Power Sources* **1999,** *79*, 215-219.
7. Eftekhari, A., *J Power Sources* **2004,** *126*, 221-228.
8. Wessells, C. D.; Huggins, R. A.; Cui, Y., *Nat Commun* **2011,** *2*, 550.
9. Pasta, M.; Wessells, C. D.; Huggins, R. A.; Cui, Y., *Nat Commun* **2012,** *3*, 1149.
10. Kim, D. J.; Jung, Y. H.; Bharathi, K. K.; Je, S. H.; Kim, D. K.; Coskun, A.; Choi, J. W., *Adv Energy Mater* **2014,** *4*, 1400133.
11. Pasta, M.; Wang, R. Y.; Ruffo, R.; Qiao, R.; Lee, H.-W.; Shyam, B.; Guo, M.; Wang, Y.; Wray, L. A.; Yang, W., *Journal of Materials Chemistry A* **2016,** *4*, 4211-4223.
12. Lu, Y.; Wang, L.; Cheng, J.; Goodenough, J. B., *Chem Commun (Camb)* **2012,** *48*, 6544-6.
13. Asakura, D.; Li, C. H.; Mizuno, Y.; Okubo, M.; Zhou, H.; Talham, D. R., *J Am Chem Soc* **2013,** *135*, 2793-9.
14. Wang, L.; Lu, Y.; Liu, J.; Xu, M.; Cheng, J.; Zhang, D.; Goodenough, J. B., *Angew Chem Int Ed Engl* **2013,** *52*, 1964-7.
15. Yue, Y.; Binder, A. J.; Guo, B.; Zhang, Z.; Qiao, Z. A.; Tian, C.; Dai, S., *Angew Chem Int Ed Engl* **2014,** *53*, 3134-7.
16. Lee, H. W.; Wang, R. Y.; Pasta, M.; Woo Lee, S.; Liu, N.; Cui, Y., *Nat Commun* **2014,** *5*, 5280.
17. Wang, L.; Song, J.; Qiao, R.; Wray, L. A.; Hossain, M. A.; Chuang, Y. D.; Yang, W.; Lu, Y.; Evans, D.; Lee, J. J.; Vail, S.; Zhao, X.; Nishijima, M.; Kakimoto, S.; Goodenough, J. B., *J Am Chem Soc* **2015,** *137*, 2548-54.
18. Wessells, C. D.; McDowell, M. T.; Peddada, S. V.; Pasta, M.; Huggins, R. A.; Cui, Y., *ACS Nano* **2012,** *6*, 1688-94.
19. Wessells, C. D.; Peddada, S. V.; McDowell, M. T.; Huggins, R. A.; Cui, Y., *J. Electrochem. Soc* **2011,** *159*, A98-A103.
20. You, Y.; Yu, X. Q.; Yin, Y. X.; Nam, K. W.; Guo, Y. G., *Nano Research* **2015,** *8*, 117-128.
21. Lim, S. Y.; Lee, J. H.; Kim, S.; Shin, J.; Choi, W.; Chung, K. Y.; Jung, D. S.; Choi, J. W., *Acs Energy Letters* **2017,** *2*, 998-1004.
22. Mitchell, J. B.; Lo, W. C.; Genc, A.; LeBeau, J.; Augustyn, V., *Chem Mater* **2017,** *29*, 3928-3937.
23. Nam, K. W.; Kim, S.; Yang, E.; Jung, Y.; Levi, E.; Aurbach, D.; Choi, J. W., *Chem Mater* **2015,** *27*, 3721-3725.
24. Wang, R.; Chung, C. C.; Liu, Y.; Jones, J. L.; Augustyn, V., *Langmuir* **2017,** *33*,

9314-9323.
25. Nam, K. W.; Kim, S.; Lee, S.; Salama, M.; Shterenberg, I.; Gofer, Y.; Kim, J. S.; Yang, E.; Park, C. S.; Kim, J. S.; Lee, S. S.; Chang, W. S.; Doo, S. G.; Jo, Y. N.; Jung, Y.; Aurbach, D.; Choi, J. W., *Nano Lett* **2015,** *15*, 4071-9.
26. Song, J.; Wang, L.; Lu, Y.; Liu, J.; Guo, B.; Xiao, P.; Lee, J. J.; Yang, X. Q.; Henkelman, G.; Goodenough, J. B., *J Am Chem Soc* **2015,** *137*, 2658-64.
27. Qiao, R.; Li, Q.; Zhuo, Z.; Sallis, S.; Fuchs, O.; Blum, M.; Weinhardt, L.; Heske, C.; Pepper, J.; Jones, M.; Brown, A.; Spucces, A.; Chow, K.; Smith, B.; Glans, P. A.; Chen, Y.; Yan, S.; Pan, F.; Piper, L. F.; Denlinger, J.; Guo, J.; Hussain, Z.; Chuang, Y. D.; Yang, W., *Rev Sci Instrum* **2017,** *88*, 033106.
28. Qiao, R. M.; Chin, T.; Harris, S. J.; Yan, S. S.; Yang, W. L., *Current Applied Physics* **2013,** *13*, 544-548.
29. Yang, W. L.; Liu, X. S.; Qiao, R. M.; Olalde-Velasco, P.; Spear, J. D.; Roseguo, L.; Pepper, J. X.; Chuang, Y.; Denlinger, J. D.; Hussain, Z., *Journal of Electron Spectroscopy and Related Phenomena* **2013,** *190*, 64-74.
30. Qiao, R. M.; Dai, K. H.; Mao, J.; Weng, T. C.; Sokaras, D.; Nordlund, D.; Song, X. Y.; Battaglia, V. S.; Hussain, Z.; Liu, G.; Yang, W. L., *Nano Energy* **2015,** *16*, 186-195.
31. Qiao, R.; Liu, J.; Kourtakis, K.; Roelofs, M. G.; Peterson, D. L.; Duff, J. P.; Deibler, D. T.; Wray, L. A.; Yang, W., *J Power Sources* **2017,** *360*, 294-300.
32. Liu, X.; Liu, J.; Qiao, R.; Yu, Y.; Li, H.; Suo, L.; Hu, Y. S.; Chuang, Y. D.; Shu, G.; Chou, F.; Weng, T. C.; Nordlund, D.; Sokaras, D.; Wang, Y. J.; Lin, H.; Barbiellini, B.; Bansil, A.; Song, X.; Liu, Z.; Yan, S.; Liu, G.; Qiao, S.; Richardson, T. J.; Prendergast, D.; Hussain, Z.; de Groot, F. M.; Yang, W., *J Am Chem Soc* **2012,** *134*, 13708-15.
33. Liu, X.; Wang, D.; Liu, G.; Srinivasan, V.; Liu, Z.; Hussain, Z.; Yang, W., *Nat Commun* **2013,** *4*, 2568.
34. Qiao, R. M.; Wang, Y. S.; Olalde-Velasco, P.; Li, H.; Hu, Y. S.; Yang, W. L., *J Power Sources* **2015,** *273*, 1120-1126.
35. Li, Q. H.; Qiao, R. M.; Wray, L. A.; Chen, J.; Zhuo, Z. Q.; Chen, Y. X.; Yan, S. S.; Pan, F.; Hussain, Z.; Yang, W. L., *J Phys D Appl Phys* **2016,** *49*, 413003.
36. Hocking, R. K.; Wasinger, E. C.; de Groot, F. M.; Hodgson, K. O.; Hedman, B.; Solomon, E. I., *J Am Chem Soc* **2006,** *128*, 10442-51.
37. Nanba, Y.; Asakura, D.; Okubo, M.; Zhou, H.; Amemiya, K.; Okada, K.; Glans, P. A.; Jenkins, C. A.; Arenholz, E.; Guo, J., *Phys Chem Chem Phys* **2014,** *16*, 7031-6.
38. Shimamoto, N.; Ohkoshi, S.; Sato, O.; Hashimoto, K., *Inorg Chem* **2002,** *41*, 678-84.
39. Kumar, A.; Yusuf, S. M.; Keller, L., *Phys Rev B* **2005,** *71*, 054414.
40. Kim, D.; Hwang, T.; Lim, J. M.; Park, M. S.; Cho, M.; Cho, K., *Phys Chem Chem Phys* **2017,** *19*, 10443-10452.
41. De Groot, F.; Kotani, A., *Core level spectroscopy of solids*. CRC press: London, 2008.
42. Liu, X.; Wang, Y. J.; Barbiellini, B.; Hafiz, H.; Basak, S.; Liu, J.; Richardson, T.;

Shu, G.; Chou, F.; Weng, T. C.; Nordlund, D.; Sokaras, D.; Moritz, B.; Devereaux, T. P.; Qiao, R.; Chuang, Y. D.; Bansil, A.; Hussain, Z.; Yang, W., *Phys Chem Chem Phys* **2015,** *17*, 26369-77.
43. Hodgman, C. D., *Handbook of Chemistry and Physics*. CRC Press: Florida, 1951; Vol. 71.
44. Zhao, L.; Yu, X. Q.; Yu, J. Z.; Zhou, Y. N.; Ehrlich, S. N.; Hu, Y. S.; Su, D.; Li, H.; Yang, X. Q.; Chen, L. Q., *Adv Funct Mater* **2014,** *24*, 5557-5566.
45. Martha, S. K.; Grinblat, J.; Haik, O.; Zinigrad, E.; Drezen, T.; Miners, J. H.; Exnar, I.; Kay, A.; Markovsky, B.; Aurbach, D., *Angew Chem Int Ed Engl* **2009,** *48*, 8559-63.
46. Muraliganth, T.; Manthiram, A., *J Phys Chem C* **2010,** *114*, 15530-15540.
47. Jørgensen, C. K., *Absorption spectra and chemical bonding in complexes*. Elsevier: Cologny, 2015.

TOC Graph: